Influence of Interfacial Area on Exciton Separation and Polaron Recombination in Nanostructured Bilayer All-Polymer Solar Cells

Thomas Pfadler,[†] Mihael Coric,[†] Claudia M. Palumbiny,[‡] Andreas C. Jakowetz,[†] Karl-Philipp Strunk,[†] James A. Dorman,[†] Philipp Ehrenreich,[†] Cheng Wang,[§] Alexander Hexemer,[§] Rui-Qi Png,[⊥] Peter K. H. Ho,[⊥] Peter Müller-Buschbaum,[‡] Jonas Weickert,[*,†] and Lukas Schmidt-Mende[*,†]

[†]Department of Physics, University of Konstanz, Universitätsstr. 10, 78457 Konstanz, Germany, [‡]Lehrstuhl für Funktionelle Materialien, Physik Department E13, Technische Universität München, James-Franck-Str. 1, 85747 Garching, Germany, [§]Experimental Systems Advanced Light Source, Lawrence Berkeley National Lab, 1 Cyclotron Road, Berkeley, California 94720, United States, and [⊥]Department of Physics, National University of Singapore, Lower Kent Ridge Road, Singapore S117542, Singapore

ABSTRACT The macroscopic device performance of organic solar cells is governed by interface physics on a nanometer scale. A comb-like bilayer all-polymer morphology featuring a controlled enhancement in donor—acceptor interfacial area is employed as a model system to investigate the fundamental processes of exciton separation and polaron recombination in these devices. The different nanostructures are characterized locally by SEM/AFM, and the buried interdigitating interface of the final device architecture is statistically verified on a large area *via* advanced grazing incidence X-ray scattering techniques. The results show equally enhanced harvesting of photoexcitons in both donor and acceptor materials directly correlated to the total enhancement of interfacial area. Apart from this beneficial effect, the enhanced interface leads to significantly increased polaron recombination losses both around the open-circuit voltage and maximum power point, which is determined in complement with diode dark current characteristics, impedance spectroscopy, and transient photovoltage measurements. From these findings, it is inferred that a spatially optimized comb-like donor—acceptor nanonetwork alone is not the ideal morphology even though often postulated. Instead, the energetic landscape has to be considered. A perfect morphology for an excitonic solar cell must be spatially and energetically optimized with respect to the donor—acceptor interface.

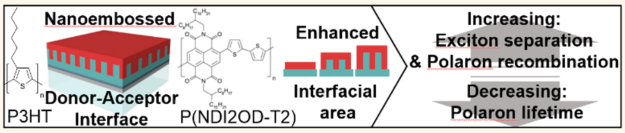

KEYWORDS: exciton separation · recombination · comb-like morphology · all-polymer · nanoimprint lithography · soft X-rays · X-ray scattering

Thin-film solar cells have the potential to deliver cheap and clean energy by converting the incident solar flux into electrical current. The mechanism of photocurrent harvesting in a solar cell is based on the photovoltaic effect that involves the generation of electrons and holes in a semiconductor device under illumination and the subsequent extraction of the charge carriers at their respective electrodes. Organic solar cells are often classified as excitonic solar cells owing to their distinctively different charge carrier separation mechanism compared to conventional p—n junction solar cells.[1] The binding energy of coulombically bound electron—hole pairs (*i.e.*, excitons) in this class of solar cells cannot be thermally overcome, and excitons need to be separated with the help of the electrochemical driving force given at a type II heterojunction.[2] In 1986, Tang presented an organic bilayer heterojunction device based on the subsequent vacuum evaporation of copper phthalocyanine (CuPc) and a perylene tetracarboxylic derivative (PV).[3] This research outlined the importance of a second organic semiconducting layer on the charge generation efficiency in organic solar cells. In 1995, Yu *et al.* elucidated the high quantum efficiency of exciton separation in blends of poly(2-methoxy-5-(2′-ethylhexyloxy)-1,4-phenylenevinylene) (MEH-PPV) and phenyl-C_{61}-butyric acid methyl ester (PCBM) at the time scale of photoinduced charge transfer across the donor—acceptor heterojunction that is more than 10^3 times faster than the radiative or nonradiative decay of photoexcitons in these systems.[4] Simultaneously,

* Address correspondence to
jonas.weickert@uni-konstanz.de,
lukas.schmidt-mende@uni-konstanz.de.

Received for review September 8, 2014
and accepted November 20, 2014.

10.1021/nn5064166

Yu *et al.* proved the concept of efficient charge separation that exclusively occurs at a type II heterojunction for an all-polymer MEH-PPV and cyano-polyphenylenevinylene (CN-PPV) bulk heterojunction (BHJ) device.[5] Detailed studies on the limiting influence of exciton diffusion, such as the spatial donor–acceptor phase separation in MEH-PPV and CN-PPV BHJ solar cells, were performed by Halls and co-workers, who recognized that the exciton diffusion range is typically 1 order of magnitude smaller than the optical absorption depth, thus limiting efficient exciton separation.[6] Brabec *et al.* further investigated the influence of phase separation in BHJ solar cells and found that the choice of solvent offers the possibility to indirectly control the macrophase separation, improving the overall device performance of BHJ solar cells.[7] The external quantum efficiency (EQE) of an organic solar cell can be expressed as a product of the efficiencies (η) of single processes involved from light absorption to current extraction.[8,9]

$$\begin{aligned}\eta(\text{EQE}) &= \eta(\text{absorption}) \times \eta(\text{IQE}) \\ &= \eta(\text{absorption}) \times \eta(\text{exciton diffusion}) \\ &\quad \times \eta(\text{exciton dissociation}) \\ &\quad \times \eta(\text{charge collection}) \end{aligned} \tag{1}$$

where η(IQE) describes the internal quantum efficiency which is determined by processes that are covered by the electronic properties of the photoactive materials and the spatial ordering of the donor–acceptor network.[10] The charge carrier harvesting in a bilayer heterojunction architecture in comparison to a BHJ device is spatially limited to excitons generated within the exciton diffusion length to the flat donor–acceptor interface. However, the perfect bicontinuous network provides direct percolation pathways for polarons to the respective electrodes. From a theoretical point of view, a bilayer heterojunction device featuring a controlled nanostructured interface is considered as the perfect donor–acceptor morphology.[10–12] He *et al.* demonstrated a solvent-assisted nanoimprint lithography (SANIL) technique that allowed the formation of nanostructured F8TBT/P3HT all-polymer bilayer devices with an outstanding power conversion efficiency of 1.9%.[13] They compared BHJ, flat bilayer, and nanopatterned bilayer all-polymer devices with feature sizes up to 25 nm on a 50 nm pitch. A direct correlation between enhanced donor–acceptor interfacial area and η(EQE) was found for the bilayer devices. Finally, it has been shown that the simultaneous enhancement in short-circuit current density (J_{sc}) and the overall device efficiency (η), extracted from standard current–voltage measurements (J–V measurements), is directly correlated to the enhancement in interfacial area.

In this work, we present new bottom-up, solution processed, nanoembossed donor–acceptor heterostructures for organic solar cells. We investigate a nanostructured bilayer system consisting of the p-type polymer poly(3-hexylthiophene-2,5-diyl) (P3HT) and the n-type polymer poly([*N*,*N*′-bis(2-octyldodecyl)naphthalene-1,4,5,8-bis(dicarboximide)-2,6-diyl]-*alt*-5,5′-(2,2′-bithiophene)) (P(NDI2OD-T2)).[14–18] This material composition serves as a well-known model system. Recently, the n-type polymer P(NDI2OD-T2) has shown impressive efficiencies up to 5.7% in combination with a near-IR donor polymer.[19] Most importantly, the complementary absorption of P(NDI2OD-T2) and P3HT facilitates the elucidation of the donor and acceptor contributions in spectrally resolved measurements. Furthermore, the tendency of P(NDI2OD-T2) to form aggregates even in solution, the necessity to use a mixture of solvents, and special temperature treatments to realize sufficient BHJ solar cells are removed through the bilayer model system.[20] A distinct donor–acceptor interface in this bottom-up solution process is realized *via* photo-cross-linking of the P(NDI2OD-T2) network and the subsequent deposition of P3HT from solution. Anodized aluminum oxide (AAO) membranes, featuring self-organized hexagonally nanopore arrays of different sizes, are used in a nanoimprint lithography (NIL) process to tailor the topography of the P(NDI2OD-T2) layer.[21,22] In addition to the common local real space characterization techniques, like scanning electron microscopy (SEM) and atomic force microscopy (AFM), a statistically averaged reciprocal space analysis method, namely, grazing incidence resonant soft X-ray scattering (GI-RSoXS), is applied to probe the quality of the nanoimprinting process and the final interdigitating structure.

For this investigation, nanostructured bilayer devices were shown to have a direct correlation between enhanced donor–acceptor interfacial area and an enhancement in EQE. As found from EQE spectra, both excitons generated in the donor as well as in the acceptor polymer equally contribute to the relative enhancement. The enhancement in EQE is subsequently visible in the corresponding J–V measurements with an increased J_{sc}. More importantly, we focus on the influence of an enhanced donor–acceptor interfacial area on polaron recombination processes for different solar cell working regimes. For this purpose, our fundamental study encloses complementary measurement techniques, such as diode dark current characteristics, transient photovoltage (TPV), and impedance spectroscopy (IS). Furthermore, our investigation shows that the controlled enhancement of donor–acceptor interfacial area on a nanometer scale is beneficial for the harvesting of photoexcitons, while simultaneously enhancing the undesired polaron recombination losses in excitonic solar cells. Finally, the measured enhancement in polaron recombination, correlated to the donor–acceptor interfacial area, potentially limits the efficiency of organic solar cells featuring the theoretically hypothesized comb-like and perfectly ordered heterostructure morphology.[11,12]

RESULTS AND DISCUSSION

A workflow description for the bottom-up synthesis of nanostructured donor–acceptor junctions employed in this study is illustrated in Figure 1. The method is generally applicable to arbitrary polymer–polymer (n-type/p-type) combinations that energetically form a type II heterostructure. Furthermore, the technique can be employed with the previous requirement for additional material compositions, such as polymer–fullerene combinations in a regular solar cell configuration.[23] However, when using a fullerene acceptor as the second layer, it is important to consider possible interdiffusion of fullerenes into the polymer layer.[24−26] It is necessary that the bottom layer consists of a polymer material in order to successfully maintain the patterned layer after photo-cross-linking.

In a NIL process, a polymer layer can be structured *in situ* and thermally developed under the influence of heat and pressure due to the temperature-dependent viscosity of polymers.[27] During molding, the polymer layer is softened and flows into the adjacent stamp structure. Subsequently, the polymer crystallizes during the cool down process, and the inverse master mold structure is transferred to the topography of the polymer film. The photo-cross-linking methodology is based on the usage of sterically hindered bis(fluorophenyl azide)s (sFPAs), whose dominant reaction is the alkyl side-chain insertion.[28] The semiconducting properties of the polymer are virtually unaffected due to the dominant alkyl side-chain insertion of the sFPA and the simultaneous suppressed insertion into π-conjugated cores. Additionally, Png and co-workers showed that the photo-cross-linking of polymers is more effective for high-molecular-mass polymers since statistically one sFPA molecule is necessary to cross-link two polymer chains.[28] The photo-cross-linking efficiency is determined by measuring gel curves that are plots of film retention as a function of cross-linker concentration.[23,28]

The workflow description in Figure 1 illustrates the specific material processing steps that are necessary to realize a solution processed all-polymer bilayer. A solution of the n-type high-molecular-weight polymer P(NDI2OD-T2) together with the sFPA additive is spin-coated on top of a glass/ITO/TiO_2 electron selective bottom support (Figure 1a). Such a device configuration, where electrons are extracted through the ITO layer, is regarded as an inverted device structure.[29,30] For our system, we chose a stiff photo-cross-linked P(NDI2OD-T2) network with around 95% film retention (Supporting Information Figure S2). Next, the glass/ITO/TiO_2/P(NDI2OD-T2) plus imprinting mold sandwich structure is placed into a mechanical hotpress. The imprinting process and an additional inside view during molding are sketched in Figure 1b,c. The thermally softened P(NDI2OD-T2) flows into the adjacent master mold structure, which is locked into the final, topographical, inverse replica of the master mold once cooled. However, at this stage, the structured n-type layer is still vulnerable and can be lost during the spin-coating of the second polymer layer. An insoluble bottom layer is fabricated by activating the sFPA cross-linker additives with deep ultraviolet light (Figure 1d). Subsequently, un-cross-linked and low-molecular-weight fractions are removed by a solvent rinse step, denoted as solvent wash in Figure 1e. The well-ordered interdigitating all-polymer morphology is finalized by spin-coating P3HT on top of the P(NDI2OD-T2) nanocolumns. Not shown in the schematic illustration of Figure 1 is the last preparation step, the thermal evaporation of a hole selective WO_3/Ag top contact.

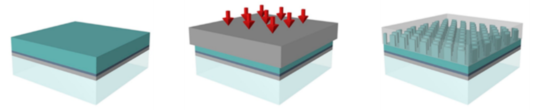

a) P(NDI2OD-T2) layer with photo-crosslinker **b)** Imprint with AAO membrane **c)** Inverse stamp structure is transferred

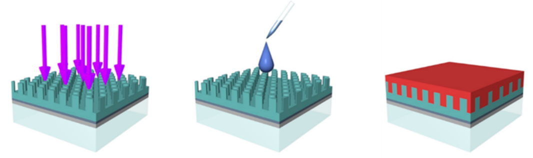

d) Activation of sFPA crosslinker with DUV light **e)** Solvent wash **f)** Application of P3HT; Nanostructured D/A all-polymer interface

Figure 1. Illustrative workflow description of nanostructured bilayer solar cells. (a) P(NDI2OD-T2) layer containing sFPA additive is spin-coated on an electron selective glass/ITO/TiO_2 bottom support. (b) AAO membrane is used as a master mold structure in a NIL process. (c) Inside view during molding; the inverse stamp structure is transferred. (d) Activation of the sFPA photo-cross-linker with deep ultraviolet (DUV) light. (e) Removal of un-cross-linked and low-molecular-weight fractions in a solvent spin rinse step; denoted as solvent wash. (f) P3HT spin-coating.

In this work, we investigate the influence of the controlled enhancement of donor–acceptor interfacial area on fundamental processes in organic solar cells. For this purpose, a comparison of a flat unstructured and two nanoimprinted architectures with an increasing donor–acceptor interface is performed. A summary of extracted geometries is given in Figure 2. SEM pictures of two different AAO membranes which serve as master mold structures in the NIL process (Figure 1b,c) are shown in the first column of Figure 2. The AAO surface formation is based on an electrochemically driven self-organizing process. The period of the highest packing density honeycomb structure can be tuned in a range of 60–500 nm through the subsequent processing conditions, and the specific pore diameter is finally tuned in an isotropic chemical etching process under controlled conditions.[21] For this study, we chose two master structures, both with the same lattice period of 100 nm, whose processing conditions only differed in terms of the final chemical etching process, thus yielding 35 nm pore diameter (Figure 2a) *versus* 75 nm pore

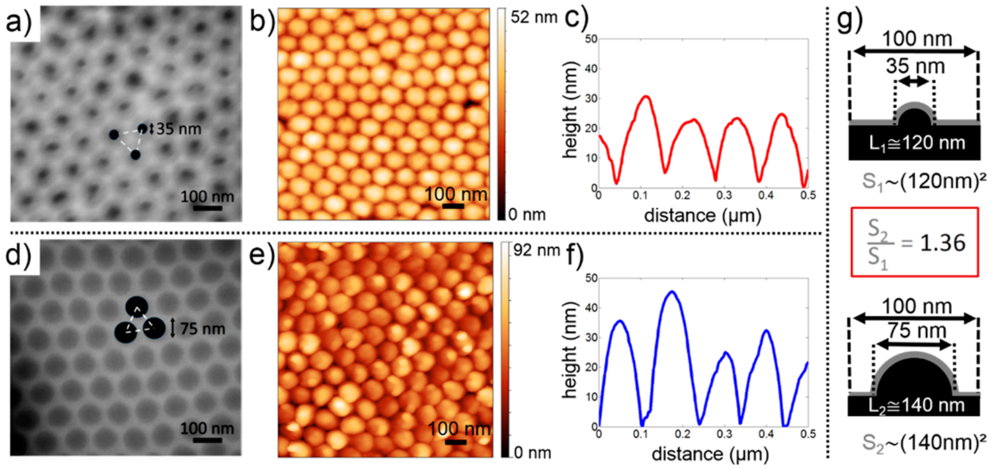

Figure 2. Comparison of extracted topographies. The 35 nm structures are shown in the first row, and the 75 nm structures are shown in the second row. Each column offers a direct comparison of the respective nanostructures. (a,d) SEM pictures of the master mold structures used in the NIL process. Both AAO membranes feature a honeycomb lattice with a periodicity of 100 nm and only differ from each other in terms of the specific pore diameter. (b,e) AFM topographic height profiles of imprinted P(NDI2OD-T2) films. (c,f) Corresponding AFM line sections are representatively shown. (g) Simplified model to give a quantitative starting point for the difference in surface area of the two employed master mold structures. The 75 nm structure is estimated to feature 36% surface enhancement over the 35 nm structure.

diameter (Figure 2d). Corresponding AFM topographic height profiles of the resulting nanopatterned P(NDI2OD-T2) films are shown in the same row (Figure 2b,e), respectively. The right-hand side of each AFM picture shows the corresponding AFM line sections (Figure 2c,f). By assuming a simple geometrical model (Figure 2g), we give a quantitative starting point for the difference in surface area of the 35 nm and the 75 nm nanopore master mold structure (Figure 2a,d,g). The 100 nm periodicity of the honeycomb lattice also is the maximum diameter of one unit cell (Figure 2g). The shape of a nanopore (Figure 2a,d) is assumed to be a hemisphere due to the nature of the isotropic etching process. The surface area (*S*) of one unit cell scales quadratically with the length (*L*) of the 1D surface line (Figure 2g) of a unit cell. This length was determined from a simple one-dimensional consideration taking the specific pore diameter and the width of the unit cell into account. By relating S_2 to S_1 (Figure 2g), the geometrical correction factors due to the 1D to 2D transition cancel out and a difference in total surface area of 36% is estimated for the 35 and 75 nm master mold structure. Liu and co-workers showed that a good solvent causes a cross-linked polymer network (P3HT with sFPA) to swell and expand.[23] Consequently, an exact value for the height of a nanocolumn in our final interdigitating donor–acceptor network is hard to determine, but the solvent wash (Figure 1e) is estimated (AFM) to cause around 65% reduction in nanocolumn height with respect to the structure size before washing (Figure S1). By spin-coating P3HT (Figure 1f) on top of the nanostructure, the film swells and expands again. Opposite to the case after solvent washing (Figure S1), the swelled nanostructure is filled with P3HT, which prevents the nanotopography from contracting. Accordingly, the final nanocolumn height at the donor–acceptor interface is expected to be smaller than measured before the solvent treatment (Figure 2b,c,e,f) but taller than the contracted topography after solvent washing (Figure S1). Further measurements like transmission electron microscopy (TEM) cross sections or TEM tomographic studies could give access to the donor–acceptor interface pattern of the final architecture, although the similarity of the two interdigitating compounds is expected to limit the contrast at the polymer–polymer interface. Nevertheless, even nanocolumn heights down to a few nanometers have a strong impact on the donor–acceptor interface physics since the exciton diffusion length of typical semiconducting polymers commonly does not exceed 10 nm.[31,32] Additionally, the overall interfacial area enhancement is affected by both the size of a single nanocolumn and the NIL large-area processability.

The previous section on local real space characterization focused on the dependency of donor–acceptor interface enhancement on the shape of single nanopillars (Figure 2). The overall surface enhancement due to the structuring of the P(NDI2OD-T2) layer is additionally determined by the large-area processability due to the NIL process. Finally, the preservation of the distinct donor–acceptor interface after solution casting of the second polymeric layer is crucial for the overall device performance. Advanced scattering techniques like grazing incidence small-angle scattering (GISAXS) give access to statistically averaged structure information on an illuminated real space area comparable to the size of our organic solar cells.[33] In this study, we characterized structured P(NDI2OD-T2) layers featuring the 75 nm structure (Figure 2) with GI-RSoXS and GISAXS.[33,34] Measurements were performed at the synchrotron beamlines 11.0.1.2 and 7.3.3 of the Advanced

Light Source (ALS) in Lawrence Berkeley National Lab (USA) and offer the possibility to probe samples at material specific resonant scattering features.[35−37] Hard X-ray GISAXS measurements statistically verified the large-area processability due to the NIL process when investigating imprinted P(NDI2OD-T2) films without a P3HT capping layer.[38] However, the buried interdigitating donor−acceptor interface after deposition of the second polymeric layer could not be resolved (Figure S7).

RSoXS shares many advantages with GISAXS in characterizing the morphology of a large variety of materials.[33,39−43] For characterizing the structure of organic soft matter with hard X-rays, the contrast of scattering between two materials relies on the difference in electron densities in the first and second material.[33] In the case of P(NDI2OD-T2):P3HT, this electron density difference gives insufficient contrast between the materials.[44] With RSoXS and the possibility of varying the energy of the soft X-rays, one can yield chemical contrast between the two components near the absorption edge for specific elements.[39,40,45−47] This contrast arises due to differences in the chemical structures reflected as the complex refractive indices of P(NDI2OD-T2) and P3HT. Traces of the resonant first-order scattering feature (Figure 3c) that coincides with the first-order feature of the structured P(NDI2OD-T2) without P3HT on top (Figure 3a) could be observed by minimizing diffuse scattering from the P3HT−air(vacuum) interface.[48] The strongest contrast was found at an energy of 283.8 eV. The comparably weak scattering signal shown in Figure 3c is attributed to a weak contrast between P(NDI2OD-T2) and P3HT rather than a structural damage of the nanopattern upon solution coating. In order to verify this, a polystyrene (PS) homopolymer, instead of P3HT, was solution-coated on the P(NDI2OD-T2) structure. The difference in refractive index between P(NDI2OD-T2) and PS is higher in comparison to P(NDI2OD-T2) and P3HT at an energy of 283.8 eV. Samples with PS on P(NDI2OD-T2) show resonant first- and second-order scattering features (Figure 3b) due to the honeycomb structured interface and significantly more contrast. This becomes apparent when exemplarily comparing the amplitudes of the first-order scattering feature for the three samples without capping layer, with P3HT and with PS in the horizontal cut plot summary of Figure 3d. Hexagonal scattering is observed up to the third order, which is strong evidence for a good ordering over the whole illuminated area, that is, the large-area processability due to the NIL process. Each point, and thereby each scattering peak position of the nanostructured P(NDI2OD-T2) (shown in Figure 3d and summarized in Table 1), corresponds to a set of lattice planes in the real space that are represented for the master mold structure in Figure 3e. From the spacing of the real space planes, the pillar-to-pillar spacing of 103.7 nm (inset of Figure 3e) is calculated from scattering along the (10) lattice axis.

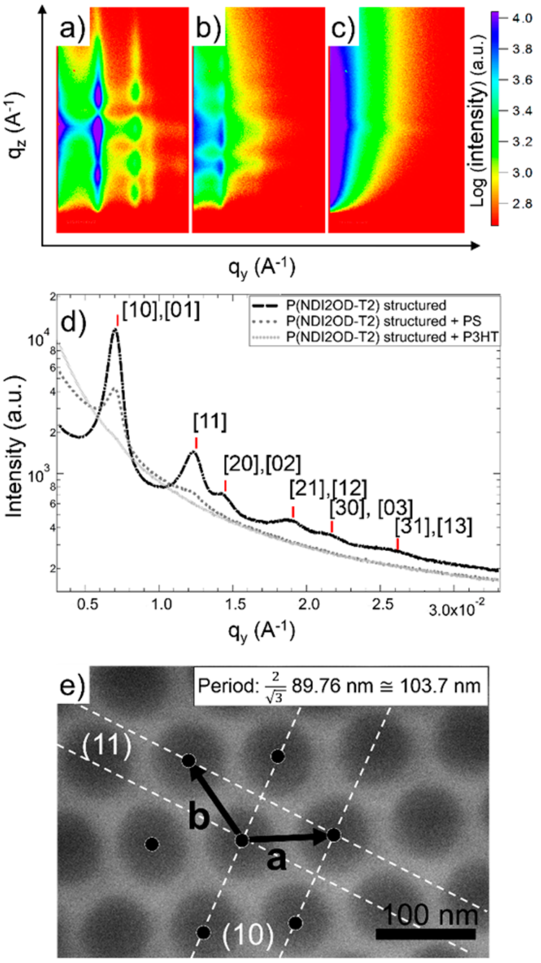

Figure 3. GI-RSoXS reciprocal space analysis of the hexagonally structured polymer−polymer interface. Scattering patterns originating from the imprinted P(NDI2OD-T2) film without capping layer (a), with solution-coated PS homopolymer on top (b) and with solution-coated P3HT on top (c). The logarithmic scale of the scattering intensity is in arbitrary units. Red represents low intensity, and blue represents high intensity. A horizontal cut summary of the three different architectures with the corresponding Miller indices is given in (d) and further summarized in Table 1. The (10) and (11) scattering planes originating from the 2D AAO honeycomb master mold structure are highlighted in (e). A period of 103.7 nm is calculated from the (10) scattering plane (inset of e).

TABLE 1. Reciprocal Scattering Peaks (*q*), Real Space Lattice Parameters (*D*) of the Imprinted 2D Honeycomb Lattice, and the Ratio of Higher-Order Peak Positions Corresponding to a 2D Hexagonal Packing (2D HXP) Arrangement[a]

[*hk*]	[10],[01]	[11]	[20],[02]	[21],[12]	[30],[03]	[31],[13]
q [nm^{-1}]	0.070	0.121	0.140	0.185	0.210	0.252
D [nm]	89.76	51.83	44.88	33.96	29.92	24.89
2D HXP ratio	1	$\sqrt{3}$	2	$\sqrt{7}$	3	$\sqrt{13}$

[a] Scattering features up to the third order (Figure 3) are measured by GI-RSoXS on nanostructured P(NDI2OD-T2) layers that feature a 75 nm topography (Figure 2e,f) with a spacing of 103.7 nm calculated from the scattering results according to Figure 3e.

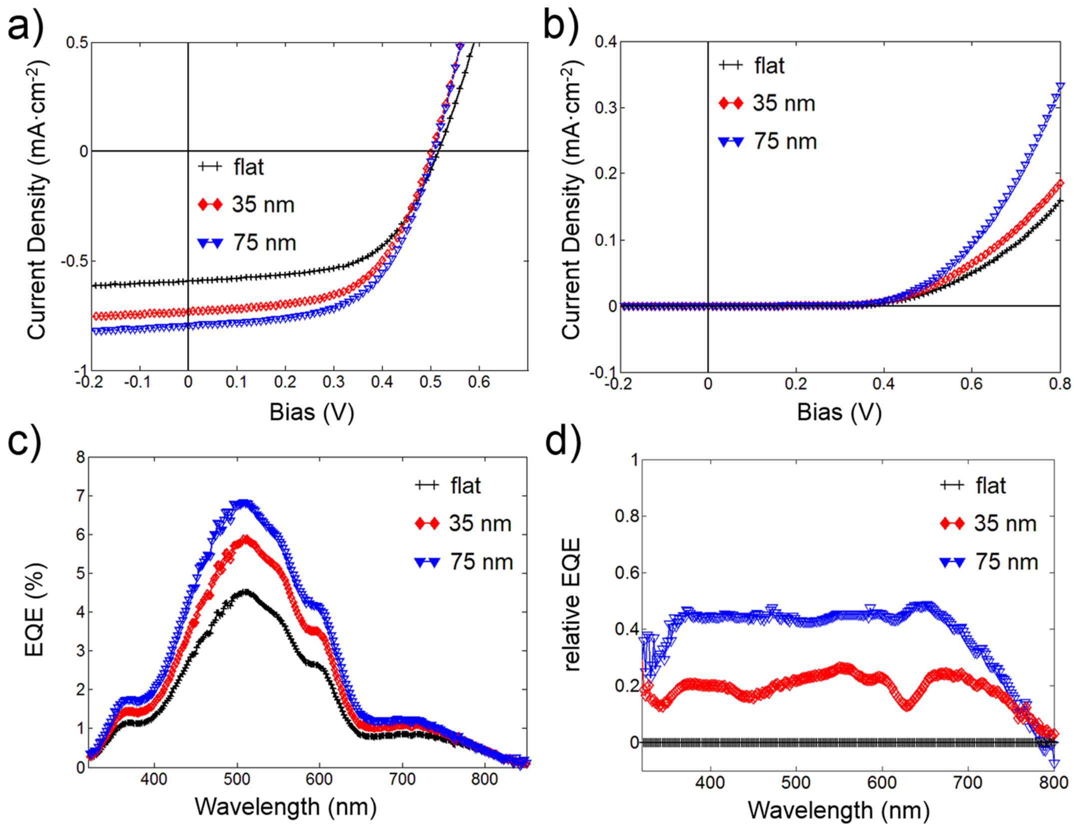

Figure 4. Representative *J*−*V* and EQE characteristics of comb-like bilayer devices featuring an enhancement in interfacial area. (a) *J*−*V* characteristics recorded under simulated AM 1.5G solar illumination. (b) Diode dark current characteristics emphasizing polaron recombination in forward direction. (c) Corresponding EQE of nanostructured devices. (d) Relative EQE enhancement: [EQE(structured) − EQE(flat)]/EQE(flat).

Results from the GI-RSoXS characterization of the nanostructured bilayer architectures show that the NIL process of the first polymer layer in combination with solution casting of the second layer is successful over the whole imprinted surface. At the same time, the absence of contrast in hard GISAXS scattering (Figure S7) is indicative of two important aspects. First, it is direct evidence that the filling of the P3HT into the nanostructured P(NDI2OD-T2) is complete. Additionally, it demonstrates that the periodic patterning of the polymer/polymer interface is not transferred to the P3HT/air(vacuum) interface, indicating that the geometry of the Ag back-electrode is independent of the patterned bilayer interface. Note that air enclosures both at the interface and the structured P3HT/air-(vacuum) interface would dramatically increase coherent scattering reflected in strong scattering features.

The performance of excitonic solar cells is drastically influenced by the spatial ordering, a type II heterostructure energy level alignment of donor and acceptor, and the total donor−acceptor interfacial area. In this work, we prepared nanoembossed bilayer, all-polymer solar cells with a distinct and enhanced donor−acceptor interface (Figures 1 and 2). The complementary absorption (Figure S3) of the n-type P(NDI2OD-T2) and the p-type P3HT together with the well-ordered, bicontinuous morphology featuring a controlled enhancement in interfacial area allows the investigation of the influence of the donor−acceptor interfacial area on fundamental polaron generation and recombination processes in our model system for a comb-like all-polymer device. Different complementary solar cell characterization techniques, focusing at different working regimes of the excitonic solar cells, are presented and discussed in the following sections.

TABLE 2. Characteristic Solar Cell Parameters Recorded under Simulated AM 1.5G Solar Irradiance[a]

	V_{OC} (mV)	J_{sc} (mA cm^{-2})	FF (%)	η (%)
flat	515	−0.59	58	0.18
35 nm	501	−0.73	57	0.21
75 nm	506	−0.80	58	0.23

[a] The values are extracted from the *J*−*V* characteristics shown in Figure 4a.

The results of the *J*−*V* and the EQE measurements are plotted in Figure 4. Inverted all-polymer solar cells featuring a flat, a 35 nm, and a 75 nm pore diameter structure were examined (Figure 2). The results of representative *J*−*V* measurements under simulated AM 1.5G solar illumination are plotted in Figure 4a, and the corresponding characteristic solar cell parameters are summarized in Table 2. Additional results for nanostructured bilayer solar cells, BHJ devices, a comparison to literature values, and details on data evaluation are given in the Supporting Information.

There are three different working regimes of the solar cells shown in Figure 4a. Starting at negative bias, the crossing point of a *J*−*V* characteristic with the vertical current density axis is denoted as short-circuit current density J_{sc}.[49] At zero bias, in good approximation, no charge carriers are injected through the electrodes and only photogenerated charge carriers contribute to the measured current. The origin of the J_{sc} in excitonic solar cells is the photoinduced charge transfer across the donor−acceptor heterojunction.[4] The generated photocurrent in our model system is directly correlated to the enhancement in donor−acceptor interfacial area, the origin of which will be discussed in more detail with the spectrally resolved EQE measurement.

The area covered by the fourth quadrant of the *J*−*V* plot is the regime where a photovoltaic device generates power.[49] The crossing point of an *J*−*V* characteristic with the horizontal bias axis is denoted as the open-circuit voltage V_{oc}.[49] The origin of the V_{oc} is still a hot topic in the organic solar cell community, but a detailed discussion of theoretical approaches that describe the V_{oc} is beyond the scope of this paper. However, from a device point of view, the value of the V_{oc} that is extracted from a *J*−*V* measurement mirrors the point at which the device is in a dynamic steady state between photogenerated charge carriers and charge carriers that are injected through the electrodes since there is no net current in the electrical circuit. Values of the V_{oc} for the different geometries are summarized in Table 2. The flat reference shows the highest V_{oc} of 515 mV and a significantly lower slope in the forward direction (bias larger than the V_{oc}) than the 35 and 75 nm structure. This is a first indication of enhanced recombination in the nanostructured devices since a dependency of the V_{oc} on dynamic processes like interface recombination is already known from literature.[50−52] It is important to note that the effect of enhanced photocurrent and increased recombination is indicative for an enhanced donor−acceptor interfacial area. A similar trend in *J*−*V* characteristics (Figure S4 and Table S1) was found by tuning the interfacial area *via* back-infiltration of P3HT into P(NDI2OD-T2) devices following the procedure of Liu *et al.*[23]

In order to simplify the discussion of the nanostructured bilayer devices at the V_{oc} and further focus on the forward bias working regime, photogenerated charge carriers are excluded by measuring the diode dark current characteristics (Figure 4b). If a forward bias larger than the injection barrier is applied, the electrodes effectively inject charges into the organic bilayer device. If these injected charges (*i.e.*, polarons) recombine radiatively, the device works as a LED.[53] The higher the slope of the diode characteristic in forward direction, the higher the polaron recombination yield (radiative and nonradiative) in the device. The diode dark current characteristics shown in Figure 4b mirror a direct correlation between polaron recombination and an enhancement in interfacial donor−acceptor area due to the NIL process. It has to be stressed that the difference in device performance is not induced by the NIL process itself but by the effectively enhanced interfacial area (Figure 4a *vs* Figure S4) that is maintained after the processing route (Figure 1). Furthermore, the direct correlation between the enhanced interfacial area and polaron recombination in the forward direction appears to be insensitive on the alignment of the donor−acceptor interface (parallel or perpendicular) with respect to the external electric field. This becomes obvious considering that the projection of the interface perpendicular to the external field is identical for the flat and the nanostructured interfaces. However, it is not verified so far whether the dominant interface recombination channel is trap-assisted recombination or bimolecular recombination.[54,55]

From a theoretical point of view, the EQE of a nanostructured bilayer heterojunction solar cell can be expressed according to eq 1. The measurement is performed under short-circuit conditions; no charge carriers are injected through the electrodes, and the photogenerated current is spectrally resolved. The EQE measurement illustrated in Figure 4c shows a direct correlation between donor−acceptor interfacial area and η(EQE). The direct relation between the spectrally resolved photogenerated current density (Figure 4c) and the J_{sc} (Figure 4a) is verified. By assuming η(absorption) being independent of the donor−acceptor interface texturing, the enhancement in η(EQE) can be directly addressed at an enhancement in η(IQE), that is, enhanced harvesting of photoexcitons from exciton diffusion to charge carrier collection (eq 1). Steady-state photoluminescence (PL) measurements (Figure S8) show reduced radiative recombination of excitons correlated to the enhancement in donor−acceptor interfacial area. The integrated PL signal for the 35 and 75 nm structure relative to the flat reference structure is 84 and 74%, respectively, when exciting P3HT at 510 nm.

The relative EQE enhancement (Figure 4d), together with the knowledge of the complementary absorption of our model system (Figure S3), allows for the interpretation of the fundamental processes of exciton separation that exclusively occurs at the nanostructured P(NDI2OD-T2):P3HT heterojunction. The relative EQE enhancement is wavelength-independent, and all three absorption features the characteristic P(NDI2OD-T2) (at around 400 and 700 nm) and the P3HT (at around 550 nm) equally contribute and directly correlate with the enhancement in interfacial area. Enhanced photoexciton harvesting, originating from both P(NDI2OD-T2) and P3HT, contributes to the enhancement in η(EQE) (Figure 4c) and consequently to the increased J_{sc} shown in Figure 4a. The J_{sc} (Table 2) for the 75 and 35 nm device is 35 and 24% higher than for the flat reference device, respectively. This is consistent with the measured 26 and 16% lower photoluminescence signal (Figure S8) with respect to the flat interface sample. When directly comparing the 75 and 35 nm devices, a surface enhancement of 36% (Figure 2) enhances the overall PL quenching by 11% and the J_{sc} by 9%.

The results of the transient photovoltage (TPV) measurements are shown in Figure 5. The technique allows for the investigation of the influence of the enhanced donor–acceptor interfacial area on polaron recombination kinetics directly in the time domain. A schematic illustration of the measurement technique is given in Figure 5a. Devices are illuminated using a 100 mW·cm^{-2} AM 1.5G solar simulator ("light-biased"), and a quasi-open-circuit condition is established by suppressing a net current flow in the electrical circuit due to the 1 MΩ termination resistance of the oscilloscope.[56] A laser pulse (Figure 5a) introduces a small optical perturbation, polarons are generated, and the disturbed system is simultaneously forced to equilibrate since additionally generated polarons recombine in the active layer of the device due to the high termination resistance, which does not allow charge collection *via* the external electrodes. Time-resolved polaron recombination is determined by monitoring the TPV decay rate with an oscilloscope. The results of the polaron recombination kinetics are plotted in Figure 5b. The inset summarizes the monoexponential fit to the extracted polaron decay kinetics (with the recombination rate (k) as a fit parameter). The inverse value of the estimated k is denoted as the polaron lifetime (τ).[57] Results of the TPV measurements are summarized in Table 3. By increasing the donor–acceptor interfacial area, the corresponding polaron lifetime under quasi-open-circuit conditions is decreased from 13.0 μs (flat reference) over 11.6 μs (35 nm structure) to 9.98 μs (75 nm structure). The controlled enhancement in interfacial area causes increased polaron recombination rates, which consistently outbalance the increased charge carrier generation rates under open-circuit conditions, where there is no net current generation.[58]

Impedance spectroscopy gives experimental access to characterize our model system under working conditions. The bias region around the maximum power point is of greatest interest since all dynamic excitonic and polaronic processes—generation, transport, and recombination—contribute to the overall device performance. For this purpose, devices are illuminated and the frequency-dependent impedance is recorded for a range of dc applied biases that cover the power generation regime of the nanostructured bilayer devices. A cole–cole plot (Figure 6a) is a complex plane representation of the imaginary (Z'') and the real part (Z') of the impedance response. The measurement

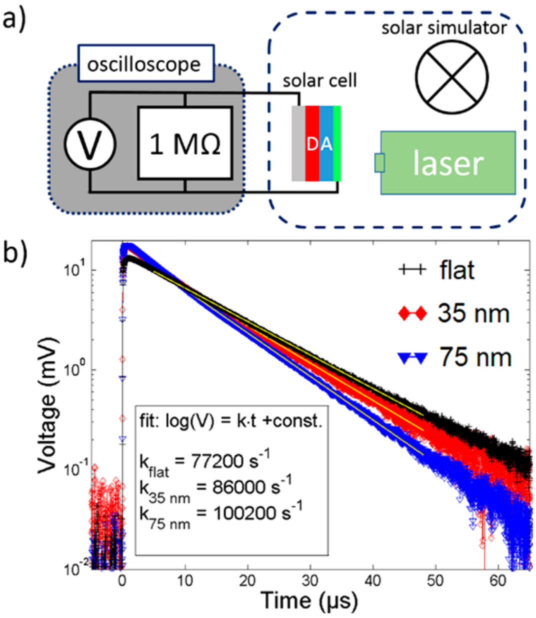

Figure 5. (a) Schematic illustration of the TPV setup. Devices are "light-biased" using a 100 mW·cm^{-2} AM 1.5G solar simulator, a small optical perturbation is introduced (532 nm laser pulse) and subsequent polaron recombination kinetics back to equilibrium is monitored with an oscilloscope. (b) TPV measurements correlated with an enhancement in donor–acceptor interfacial area. The inset summarizes the results of the monoexponential fits.

TABLE 3. Fitted TPV Decay Rates *k* and Corresponding ($\tau \equiv k^{-1}$) Polaron Lifetimes τ[a]

	k (s^{-1})	τ (μs)
flat	77200	13.0
35 nm	86000	11.6
75 nm	100200	9.98

[a] The measurement is shown in Figure 5.

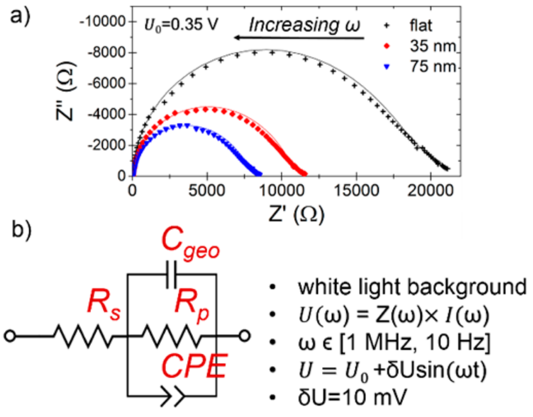

Figure 6. IS on nanostructured all-polymer devices. (a) Representative cole–cole plot of acquired frequency-dependent impedance data (symbols) with corresponding fits (solid line). (b) Equivalent circuit model that is used to fit the data points and an overview of important measurement parameters.

conditions and a representative cole–cole plot are summarized in Figure 6. The equivalent circuit (Figure 6b) that is used to fit (solid lines in Figure 6a) the experimental data needs to be highlighted since the dependency of the donor–acceptor interfacial area on recombination kinetics is based on discussing the electrical components of this circuit (Figure 7). The simple equivalent circuit shown in Figure 6b that is used to model the acquired data consists of a resistor (R_s) in series with a geometrical capacitor (C_{geo}), a resistor (R_p), and a constant phase element (CPE) in parallel. In general, the most fundamental model that can be applied to describe a solar cell is known to be a resistor in series with an R–C element.[59] Leever and coworkers successfully applied this simple model to an organic single-layer (P3HT) solar cell and further developed it to model P3HT:PCBM BHJ devices.[60] The model we employ to describe all-polymer bilayer devices is the simplest one extended by a CPE in parallel to the R–C element (Figure 6b). The additional CPE is necessary to accurately model low-frequency (ω) data points shown in the cole–cole plot (Figure 6a). The R_s circuit element represents resistive losses due to the electric contacting and charge transport through the electrodes. The capacitor C_{geo} is determined to be a geometrical capacitor whose value is calculated by assuming the equation for a simple parallel plate capacitor. The capacitance of the three thin-film solar cells with different interface geometry is calculated to be 3.7 nF by taking the device area of 0.168 cm^2, the spacing between ITO and Ag (50 nm TiO_2/60 nm P(NDI2OD-T2) and 60 nm P3HT), a dielectric constant (ε) of 31 for the anatase TiO_2, and a dielectric constant (ε) of 3 for the organic bilayer into account.[61,62] Note that the geometry of the polymer–polymer interface does not influence the geometrical capacitance due to the (supposedly) identical dielectric constants in the materials. Since the nanoimprint only introduces an ordered structure to the interface but maintains the volume of both P(NDI2OD-T2) and P3HT, the combined capacitance of the polymer layer stack would not change even for differences in the dielectric constants. The calculated value of 3.7 nF coincides with the values extracted from impedance fits shown in Figure 7a. C_{geo} is essentially independent of both bias and polymer–polymer interface structuring that is additionally consistent with the idea of a purely geometrical origin of this capacitor in the equivalent circuit. In correlation with the GISAXS measurements (Figure S7), the similarity of C_{geo} for the flat and the structured devices gives additional experimental evidence that the geometry of the Ag back-electrode is independent of the patterned bilayer interface. The extracted key parameter of the IS measurement is the recombination resistance (R_p) that describes polaron recombination under working conditions. The recombination resistance as a function of the applied bias ranging from 0.20 to 0.45 V covering the power generation regime (compare to Figure 4a) is shown for the different donor–acceptor interface patterns. As seen in the figure, the recombination resistance decreases for increasing interfacial area for all bias voltages around the maximum power point. This finding is in good accordance with the TPV results describing the situation at open-circuit conditions, where polaron extraction is suppressed as well as with dark J–V measurements characterizing the polaron injection regime.

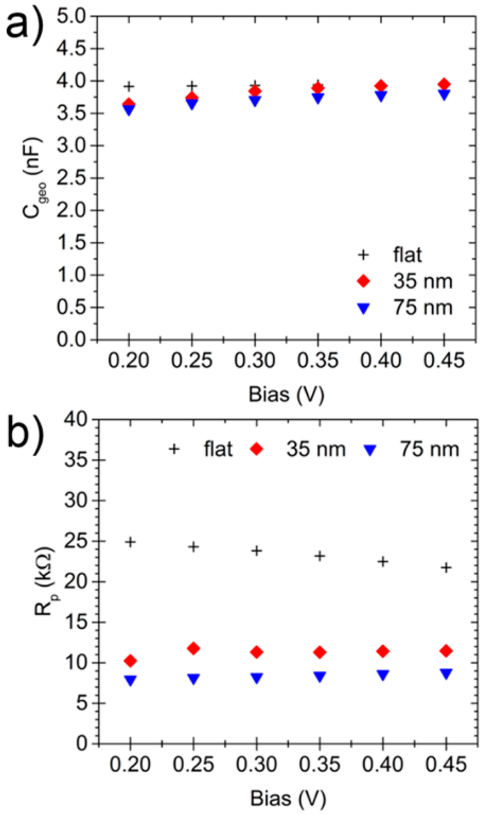

Figure 7. Electrical components of the equivalent circuit that corresponds to the IS measurement summarized in Figure 6. The geometrical capacitance C_{geo} (a) in parallel with the recombination resistance R_p (b). The geometrical capacitance is essentially independent of the polymer–polymer texturing that is indicative for two important aspects: the volume of the active material is conserved, and the interface structuring is not transferred to the Ag back-electrode.

The extracted polaron lifetimes from the TPV measurement under quasi-open-circuit conditions ranging from 13 to 9.98 μs are within the range of non-optimized P3HT:PCBM BHJ solar cells under working conditions varying from 7.8 to 22 μs that is known from literature.[60]

CONCLUSION

The presented synthesis strategy for all-solution processed nanostructured bilayer solar cells allows the controlled enhancement of donor–acceptor interfacial area in all-polymer devices. This enables the investigation of fundamental exciton separation and polaron recombination processes in a comb-like donor–acceptor architecture that has often been considered as ideal for excitonic solar cells. Our bottom-up synthesized devices feature nanopatterned donor–acceptor interfaces with very good control over the size of the employed nanostructures. Anodized aluminum oxide membranes are used in a nanoimprint lithography process to tailor the topography of the organic bottom layer. The nanostructured bottom layer is developed *via* photo-cross-linking, which allows the subsequent solution processing of the second polymer. Nanostructure topographies have been consistently characterized both locally and globally using SEM/AFM and GI-RSoXS/GISAXS, respectively. The origin of an improvement in device performance of nanostructured over flat bilayer devices is directly correlated to the enhancement in donor–acceptor interfacial area. Furthermore, due to complementary spectral features of the employed model donor and acceptor polymers, it is possible to conclude from EQE results that exciton separation across the donor–acceptor interface due to both electron transfer to the acceptor as well as hole transfers to the donor equally contributes to a relative enhancement in photocurrent. Apart from improved exciton harvesting upon nanopatterning of the polymer–polymer interface, there is significant enhancement of polaron recombination correlated to the enhanced interfacial area supposedly owing to an increased number of interface states.[63] Several complementary characterization techniques focusing on different working regimes of the solar cells were employed to investigate the influence of the interface enhancement. Dark diode current characteristics show an enhanced recombination yield of injected polarons that has strong impact on the shape of the J–V characteristics. Additionally, the recombination of injected polarons in the forward direction exclusively depends on the total interfacial area and seems to be insensitive to the interface alignment with respect to the external electric field. TPV measurements consistently show that enhanced polaron generation rates are outbalanced by enhanced polaron recombination rates at the V_{oc}. Increased recombination is found not only in forward bias and at open-circuit voltage but also under solar cell working conditions around the maximum power point as inferred from impedance spectroscopy results. According to the findings of Mandoc and co-workers who investigated recombination mechanisms in all-polymer BHJ devices, we assume that the dominant recombination mechanism (at 1 sun) in our system is bimolecular recombination.[55] However, a detailed study of light-intensity-dependent current–voltage curves, which was not in the scope of this fundamental study, could give access to the exact order of the recombination.

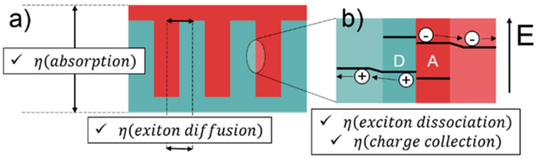

Figure 8. Illustration of the perfect comb-like morphology for a high efficiency excitonic solar cell (eq 1). A vertically optimized spacing guarantees optimized η(absorption), whereas a horizontal spacing of the donor–acceptor interfaces with respect to the exciton diffusion length guarantees optimized η(exciton diffusion). Beside the bi-continuous spatial optimization (a), the perfect morphology needs to be energetically optimized (b). In the ideal energy landscape both holes and electrons are funneled away from the interface immediately after exciton splitting through slight steps in the HOMO and LUMO levels of donor and acceptor, respectively. This can for instance be realized *via* changes in the local crystallinity or different phases as discussed by Jamieson and Burke and co-workers for polymer–fullerene bulk heterojunctions.[65,66]

The investigation of our model system shows that polaron recombination not only limits the efficiency of BHJ solar cells but also limits the efficiency of well-ordered heterostructure devices, as well.[64] In efficient polymer–fullerene BHJ solar cells, the issue of interface recombination is partly solved due to different phases (amorphous and crystalline, mixed and pure phases).[65] As discussed by Jamieson and co-workers, pure crystalline fullerene domains can act as energetic sinks for photogenerated charge carriers, which allow efficient charge collection and hinder polaron recombination.[66]

This in combination with our findings implies that the often postulated ideal comb-like donor–acceptor morphology is indeed spatially optimized (Figure 8a) in terms of absorption, exciton diffusion, and direct charge percolation pathways toward the external electrodes, but the proposed ideal morphology ignored the energy landscape (Figure 8b) which has the potential to limit recombination. Therefore, a perfect morphology for an excitonic solar cell is a multiphase (or multilayer) system as discussed by Burke *et al.* but includes the spatial arrangement, such as a comb-like geometry (Figure 8).[65]

METHODS

Device Preparation (Illustrated in Figure 1). ITO substrates (PGO, 10 $\Omega\,\square^{-1}$) were cleaned by ultrasonic bath using deionized water with dishwashing detergent, acetone, and isopropyl alcohol for at least 5 min each followed by 7 min O_2 plasma cleaning (Diener Femto). Approximately 50 nm of TiO_2 was deposited *via* spray pyrolysis of a titanium diisopropoxy bisacetonate precursor (Sigma-Aldrich) solution diluted 1:10 (vol/vol) in ethanol. Clean substrates were heated to 450 °C with a ramp rate of 30 °C/min. The precursor solution was then deposited using a spray nozzle, annealed at 450 °C for 15 min, and cooled naturally. A layer of approximately 60 nm of the n-type polymer P(NDI2OD-T2) (Polyera Corporation, M_W 100–150 kDa) layers (10 mg mL^{-1}, dissolved in xylene) containing 5 wt % sFPA additive (synthesized according to Png *et al.*) was spin-coated (45 s/1500 rpm, 15 s/2000 rpm) in a nitrogen-filled glovebox on clean glass/ITO/TiO_2 substrates.[20]

Nanoimprint lithography of P(NDI2OD-T2) films was performed with a mechanical hotpress (Collin GmbH) for 5 min at 60 °C under a pressure of 350 × 10^7 Pa. Accordingly, flat (unpatterned) P(NDI2OD-T2) films were placed on a hot plate (5 min at 60 °C) in order to maintain comparable thermal processing. The sFPA photo-cross-linker was activated by exposing the samples with a DUV (254 nm) and an approximate dose of 300 mJ cm^{-2} under controlled conditions (oxygen content below 3 ppm).

Solvent washing was realized by solvent soaking (200 μL drop) and subsequent spin-coating (1 min, 2000 rpm) of pure toluene. Solvent-washed films were kept overnight in a nitrogen-filled glovebox, equipped with a solvent absorber system. An approximately 60 nm thick layer of the p-type polymer P3HT (Merck, 10 mg mL^{-1}, dissolved in toluene) was spin-coated (45 s/1500 rpm, 15 s/2000 rpm) on top of the dried P(NDI2OD-T2) films.

Finally, a thermally evaporated top contact of 5 nm WO_3/150 nm Ag top electrodes was added to device. Evaporation was carried out at a base pressure below 5×10^{-4} Pa.

Device characterization: $J-V$ and EQE spectra were recorded using an automated LabView program controlling a Keithley 2400 sourcemeter. $J-V$ characterization under illumination was acquired using a 150 W Xe lamp solar simulator. A Frauenhofer Institute certified Si reference solar cell equipped with a KG5 filter was used for calibration. Dark diode characteristics were similarly recorded, but the devices were shielded from illumination. Spectrally resolved EQE measurements were performed using a xenon white light source focused into a grating monochromator (LOT-Oriel Omni 150) equipped with a set of appropriate edge pass filters. Cells were illuminated through a shadow mask with an illuminated area of 0.125 cm^2 according to the device characterization guidelines by Snaith.[48] For transient photovoltage measurements, a pulsed (10 Hz, 532 nm) laser with approximately 4 ns pulse length was focused onto the solar cells. Devices were background-illuminated with a solar simulator (LOT-Oriel LS0106) with an AM 1.5G solar spectrum and a light intensity of 100 mW·cm^{-2}. Signals were recorded with a digital oscilloscope (Tekscope DPO 7254) and a termination resistance of 1 MΩ was used. Impedance spectra were recorded with an Ecochemie Autolab Potentiostat/Galvanostat. Devices were illuminated with a white light diode with approximately 100 mW·cm^{-2} (adjusted using a silicon reference diode), characterized at different applied biases (0.2 V - 0.45 V) and frequencies (1 MHz−10 Hz). PL measurements were performed with a Horiba Yvon Fluorolog spectrometer with a 500 W halogen lamp.

GI-RSoXS was used at the synchrotron beamline 11.0.1.2 of the Advanced Light Source (ALS) at the Berkeley National Laboratory (LBNL) in Berkeley (USA). The measurement setup is under high vacuum due to the high absorption of soft X-rays in air. The energy of the X-rays was stepwise altered around the resonant scattering of carbon from 283 to 284 eV (4.381 to 4.366 nm) with a step size of 0.1 eV. An incident angle $\alpha_i = 5°$ was chosen for all measurements. The strongest contrast between P(NDI2OD-T2) and P3HT near the carbon K edge was found to be at 283.8 eV. The scattering signal was collected by a CCD camera with a size of 2048 pixels × 2048 pixels (pixel size of 13 μm × 13 μm). The measuring time was 20 s.

GISAXS measurements were performed at the beamline 7.3.3. at the ALS at the LBNL in Berkeley. The sample−detector distance was chosen to be 3549.24 mm using an evacuated flight tube and a Pilatus 1 M detector. The X-ray energy was 10 keV, and the incident angle was varied 0.01° from 0.1 to 0.4°. Typically, an angle of 0.16° is used under these conditions for polymeric systems.

Conflict of Interest: The authors declare no competing financial interest.

Acknowledgment. We thank Professor L.L. Chua at the National University of Singapore and her team for providing the cross-linking molecules. We acknowledge support by the German Research Foundation (DFG) in the "SPP1355: Elementary processes of organic photovoltaics" and in the project "Identification and overcoming of loss mechanisms in nanostructured hybrid solar cells—pathways toward more efficient devices". C.M. P. acknowledges the GreenTech Initiative - Interface Science for Photovoltaics (ISPV) of the EuroTech Universities together with the International Graduate School of Science and Engineering (IGSSE), TUM, and the International Doctorate Program in Nano-BioTechnology (IDK-NBT) - Elite Network of Bavaria and the Center for NanoScience (CeNS). J.A.D. acknowledges funding by the Alexander von Humboldt Foundation. The Advanced Light Source is supported by the Director, Office of Science, Office of Basic Energy Sciences, of the U.S. Department of Energy under Contract No. DE-AC02-05CH11231.

Supporting Information Available: Real (AFM) and reciprocal space (GISAXS) nanostructure characterization; P(NDI2OD-T2): sFPA film retention characteristics; complementary P(NDI2OD-T2) and P3HT absorption; back-infiltrated P(NDI2OD-T2):P3HT solar cells; P(NDI2OD-T2):P3HT BHJ solar cell; information on data evaluation and a second data set on nanostructured bilayer devices; steady-state photoluminescence quenching of nanoembossed bilayer samples. This material is available free of charge *via* the Internet at http://pubs.acs.org.

REFERENCES AND NOTES

1. Gregg, B. A. Excitonic Solar Cells. *J. Phys. Chem. B* **2003**, *107*, 4688–4698.
2. Singh, J. *Electronic and Optoelectronic Properties of Semiconductor Structures*; Cambridge University Press: Cambridge, 2003; pp 109−118.
3. Tang, C. W. Two-Layer Organic Photovoltaic Cell. *Appl. Phys. Lett.* **1986**, *48*, 183–185.
4. Yu, G.; Gao, J.; Hummelen, J.; Wudl, F.; Heeger, A. Polymer Photovoltaic Cells: Enhanced Efficiencies *via* a Network of Internal Donor−Acceptor Heterojunctions. *Science* **1995**, *270*, 1789–1790.
5. Yu, G.; Heeger, A. J. Charge Separation and Photovoltaic Conversion in Polymer Composites with Internal Donor/Acceptor Heterojunctions. *J. Appl. Phys.* **1995**, *78*, 4510–4515.
6. Halls, J. J. M.; Walsh, C. A.; Greenham, N. C.; Marseglia, E. A.; Friend, R. H.; Moratti, S. C.; Holmes, A. B. Efficient Photodiodes from Interpenetrating Polymer Networks. *Nature* **1995**, *376*, 498–500.
7. Brabec, C. J.; Sariciftci, N. S.; Hummelen, J. C. Plastic Solar Cells. *Adv. Funct. Mater.* **2001**, *11*, 15–26.
8. Park, S. H.; Roy, A.; Beaupre, S.; Cho, S.; Coates, N.; Moon, J. S.; Moses, D.; Leclerc, M.; Lee, K.; Heeger, A. J. Bulk Heterojunction Solar Cells with Internal Quantum Efficiency Approaching 100%. *Nat. Photonics* **2009**, *3*, 297–302.
9. Deibel, C.; Dyakonov, V. Polymer-Fullerene Bulk Heterojunction Solar Cells. *Rep. Prog. Phys.* **2010**, 73.
10. Watkins, P. K.; Walker, A. B.; Verschoor, G. L. B. Dynamical Monte Carlo Modelling of Organic Solar Cells: The Dependence of Internal Quantum Efficiency on Morphology. *Nano Lett.* **2005**, *5*, 1814–1818.
11. Weickert, J.; Dunbar, R. B.; Hesse, H. C.; Wiedemann, W.; Schmidt-Mende, L. Nanostructured Organic and Hybrid Solar Cells. *Adv. Mater.* **2011**, *23*, 1810–1828.
12. Coakley, K. M.; McGehee, M. D. Conjugated Polymer Photovoltaic Cells. *Chem. Mater.* **2004**, *16*, 4533–4542.
13. He, X.; Gao, F.; Tu, G.; Hasko, D.; Hüttner, S.; Steiner, U.; Greenham, N. C.; Friend, R. H.; Huck, W. T. S. Formation of Nanopatterned Polymer Blends in Photovoltaic Devices. *Nano Lett.* **2010**, *10*, 1302–1307.
14. Yan, H.; Chen, Z.; Zheng, Y.; Newman, C.; Quinn, J. R.; Dotz, F.; Kastler, M.; Facchetti, A. A High-Mobility Electron-Transporting Polymer for Printed Transistors. *Nature* **2009**, *457*, 679–686.
15. Rivnay, J.; Toney, M. F.; Zheng, Y.; Kauvar, I. V.; Chen, Z.; Wagner, V.; Facchetti, A.; Salleo, A. Unconventional Face-on Texture and Exceptional In-Plane Order of a High Mobility n-Type Polymer. *Adv. Mater.* **2010**, *22*, 4359–4363.
16. Rivnay, J.; Steyrleuthner, R.; Jimison, L. H.; Casadei, A.; Chen, Z.; Toney, M. F.; Facchetti, A.; Neher, D.; Salleo, A. Drastic Control of Texture in a High Performance n-Type Polymeric Semiconductor and Implications for Charge Transport. *Macromolecules* **2011**, *44*, 5246–5255.

17. Dang, M. T.; Hirsch, L.; Wantz, G. P3HT:PCBM, Best Seller in Polymer Photovoltaic Research. *Adv. Mater.* **2011**, *23*, 3597–3602.
18. Venkataraman, D.; Yurt, S.; Venkatraman, B. H.; Gavvalapalli, N. Role of Molecular Architecture in Organic Photovoltaic Cells. *J. Phys. Chem. Lett.* **2010**, *1*, 947–958.
19. Mori, D.; Benten, H.; Okada, I.; Ohkita, H.; Ito, S. Highly Efficient Charge-Carrier Generation and Collection in Polymer/Polymer Blend Solar Cells with a Power Conversion Efficiency of 5.7%. *Energy Environ. Sci.* **2014**, *7*, 2939–2943.
20. Schubert, M.; Dolfen, D.; Frisch, J.; Roland, S.; Steyrleuthner, R.; Stiller, B.; Chen, Z.; Scherf, U.; Koch, N.; Facchetti, A. *et al.* Influence of Aggregation on the Performance of All-Polymer Solar Cells Containing Low-Bandgap Naphthalenediimide Copolymers. *Adv. Energy Mater.* **2012**, *2*, 369–380.
21. Lee, W.; Ji, R.; Gosele, U.; Nielsch, K. Fast Fabrication of Long-Range Ordered Porous Alumina Membranes by Hard Anodization. *Nat. Mater.* **2006**, *5*, 741–747.
22. Guo, L. J. Nanoimprint Lithography: Methods and Material Requirements. *Adv. Mater.* **2007**, *19*, 495–513.
23. Liu, B.; Png, R.-Q.; Zhao, L.-H.; Chua, L.-L.; Friend, R. H.; Ho, P. K. H. High Internal Quantum Efficiency in Fullerene Solar Cells Based on Crosslinked Polymer Donor Networks. *Nat. Commun.* **2012**, *3*, 1321.
24. Treat, N. D.; Brady, M. A.; Smith, G.; Toney, M. F.; Kramer, E. J.; Hawker, C. J.; Chabinyc, M. L. Interdiffusion of PCBM and P3HT Reveals Miscibility in a Photovoltaically Active Blend. *Adv. Energy Mater.* **2011**, *1*, 82–89.
25. Bartelt, J. A.; Beiley, Z. M.; Hoke, E. T.; Mateker, W. R.; Douglas, J. D.; Collins, B. A.; Tumbleston, J. R.; Graham, K. R.; Amassian, A.; Ade, H.; *et al.* The Importance of Fullerene Percolation in the Mixed Regions of Polymer−Fullerene Bulk Heterojunction Solar Cells. *Adv. Energy Mater.* **2013**, *3*, 364–374.
26. Cates, N. C.; Gysel, R.; Dahl, J. E. P.; Sellinger, A.; McGehee, M. D. Effects of Intercalation on the Hole Mobility of Amorphous Semiconducting Polymer Blends. *Chem. Mater.* **2010**, *22*, 3543–3548.
27. Williams, M. L.; Landel, R. F.; Ferry, J. D. The Temperature Dependence of Relaxation Mechanisms in Amorphous Polymers and Other Glass-Forming Liquids. *J. Am. Chem. Soc.* **1955**, *77*, 3701–3707.
28. Png, R.-Q.; Chia, P.-J.; Tang, J.-C.; Liu, B.; Sivaramakrishnan, S.; Zhou, M.; Khong, S.-H.; Chan, H. S. O.; Burroughes, J. H.; *et al.* High-Performance Polymer Semiconducting Heterostructure Devices by Nitrene-Mediated Photocrosslinking of Alkyl Side Chains. *Nat. Mater.* **2010**, *9*, 152–158.
29. Waldauf, C.; Morana, M.; Denk, P.; Schilinsky, P.; Coakley, K.; Choulis, S. A.; Brabec, C. J. Highly Efficient Inverted Organic Photovoltaics Using Solution Based Titanium Oxide as Electron Selective Contact. *Appl. Phys. Lett.* **2006**, *89*, 233517.
30. He, Z.; Zhong, C.; Su, S.; Xu, M.; Wu, H.; Cao, Y. Enhanced Power-Conversion Efficiency in Polymer Solar Cells Using an Inverted Device Structure. *Nat. Photonics* **2012**, *6*, 591–595.
31. Stübinger, T.; Brütting, W. Exciton Diffusion and Optical Interference in Organic Donor−Acceptor Photovoltaic Cells. *J. Appl. Phys.* **2001**, *90*, 3632–3641.
32. Scully, S. R.; McGehee, M. D. Effects of Optical Interference and Energy Transfer on Exciton Diffusion Length Measurements in Organic Semiconductors. *J. Appl. Phys.* **2006**, *100*, 034907.
33. Müller-Buschbaum, P. The Active Layer Morphology of Organic Solar Cells Probed with Grazing Incidence Scattering Techniques. *Adv. Mater.* **2014**, 10.1002/adma.201304187.
34. Ruderer, M. A.; Wang, C.; Schaible, E.; Hexemer, A.; Xu, T.; Müller-Buschbaum, P. Morphology and Optical Properties of P3HT:MEH-CN-PPV Blend Films. *Macromolecules* **2013**, *46*, 4491–4501.
35. Gann, E.; Young, A.; Collins, B.; Yan, H.; Nasiatka, J.; Padmore, H.; Ade, H.; Hexemer, A.; Wang, C. Soft X-ray Scattering Facility at the Advanced Light Source with Real-Time Data Processing and Analysis. *Rev. Sci. Instrum.* **2012**, *83*, 045110.
36. Wang, C.; Hexemer, A.; Nasiatka, J.; Chan, E.; Young, A.; Padmore, H.; Schlotter, W.; Lüning, J.; Swaraj, S.; Watts, B. In Resonant Soft X-ray Scattering of Polymers with a 2D Detector: Initial Results and System Developments at the Advanced Light Source. *IOP Conf. Ser.: Mater. Sci. Eng.* **2010**, *14*, 012016.
37. Hexemer, A.; Bras, W.; Glossinger, J.; Schaible, E.; Gann, E.; Kirian, R.; MacDowell, A.; Church, M.; Rude, B.; Padmore, H. In a SAXS/WAXS/GISAXS Beamline with Multilayer Monochromator. *J. Phys.: Conf. Ser.* **2010**, *247*, 012007.
38. Müller-Buschbaum, P. Grazing Incidence Small-Angle X-ray Scattering: An Advanced Scattering Technique for the Investigation of Nanostructured Polymer Films. *Anal. Bioanal. Chem.* **2003**, *376*, 3–10.
39. Mannsfeld, S. C. X-ray Scattering: In Tune with Organic Semiconductors. *Nat. Mater.* **2012**, *11*, 489–490.
40. Collins, B.; Cochran, J.; Yan, H.; Gann, E.; Hub, C.; Fink, R.; Wang, C.; Schuettfort, T.; McNeill, C.; Chabinyc, M. Polarized X-ray Scattering Reveals Non-crystalline Orientational Ordering in Organic Films. *Nat. Mater.* **2012**, *11*, 536–543.
41. Glatter, O.; Kratky, O. *Small Angle X-ray Scattering*; Academic Press: London, 1982.
42. Roe, R.-J.; Roe, R. *Methods of X-ray and Neutron Scattering in Polymer Science*; Oxford University Press: New York, 2000.
43. Stribeck, N. *X-ray Scattering of Soft Matter*; Springer: Berlin, 2007.
44. Yan, H.; Collins, B. A.; Gann, E.; Wang, C.; Ade, H.; McNeill, C. R. Correlating the Efficiency and Nanomorphology of Polymer Blend Solar Cells Utilizing Resonant Soft X-ray Scattering. *ACS Nano* **2011**, *6*, 677–688.
45. Swaraj, S.; Wang, C.; Yan, H.; Watts, B.; Luning, J.; McNeill, C. R.; Ade, H. Nanomorphology of Bulk Heterojunction Photovoltaic Thin Films Probed with Resonant Soft X-ray Scattering. *Nano Lett.* **2010**, *10*, 2863–2869.
46. Virgili, J. M.; Tao, Y.; Kortright, J. B.; Balsara, N. P.; Segalman, R. A. Analysis of Order Formation in Block Copolymer Thin Films Using Resonant Soft X-ray Scattering. *Macromolecules* **2007**, *40*, 2092–2099.
47. Mitchell, G.; Landes, B.; Lyons, J.; Kern, B.; Devon, M.; Koprinarov, I.; Gullikson, E.; Kortright, J. Molecular Bond Selective X-ray Scattering for Nanoscale Analysis of Soft Matter. *Appl. Phys. Lett.* **2006**, *89*, 044101.
48. Materlik, G.; Sparks, C.; Fischer, K. *Resonant Anomalous X-ray Scattering: Theory and Applications*; North-Holland: Amsterdam, 1994.
49. Nelson, J. *The Physics of Solar Cells*; World Scientific: Singapore, 2003; pp 4−15.
50. Vandewal, K.; Tvingstedt, K.; Gadisa, A.; Inganas, O.; Manca, J. V. On the Origin of the Open-Circuit Voltage of Polymer-Fullerene Solar Cells. *Nat. Mater.* **2009**, *8*, 904–909.
51. Nelson, J.; Kirkpatrick, J.; Ravirajan, P. Factors Limiting the Efficiency of Molecular Photovoltaic Devices. *Phys. Rev. B* **2004**, *69*, 035337.
52. Vandewal, K.; Widmer, J.; Heumueller, T.; Brabec, C. J.; McGehee, M. D.; Leo, K.; Riede, M.; Salleo, A. Increased Open-Circuit Voltage of Organic Solar Cells by Reduced Donor−Acceptor Interface Area. *Adv. Mater.* **2014**, *26*, 3839–3843.
53. Hoppe, H.; Sariciftci, N. S. Organic Solar Cells: An Overview. *J. Mater. Res.* **2004**, *19*, 1924–1945.
54. Mandoc, M.; Kooistra, F.; Hummelen, J.; De Boer, B.; Blom, P. Effect of Traps on the Performance of Bulk Heterojunction Organic Solar Cells. *Appl. Phys. Lett.* **2007**, *91*, 263505.
55. Mandoc, M. M.; Veurman, W.; Koster, L. J. A.; de Boer, B.; Blom, P. W. M. Origin of the Reduced Fill Factor and Photocurrent in MDMO-PPV:PCNEPV All-Polymer Solar Cells. *Adv. Funct. Mater.* **2007**, *17*, 2167–2173.
56. Shuttle, C.; O'Regan, B.; Ballantyne, A.; Nelson, J.; Bradley, D.; De Mello, J.; Durrant, J. Experimental Determination of the Rate Law for Charge Carrier Decay in a Polythiophene: Fullerene Solar Cell. *Appl. Phys. Lett.* **2008**, *92*, 093311.
57. Von Roos, O. Analysis of the Photo Voltage Decay (PVD) Method for Measuring Minority Carrier Lifetimes in p-n Junction Solar Cells. *J. Appl. Phys.* **1981**, *52*, 5833–5837.

58. Koster, L.; Mihailetchi, V.; Ramaker, R.; Blom, P. Light Intensity Dependence of Open-Circuit Voltage of Polymer: Fullerene Solar Cells. *Appl. Phys. Lett.* **2005**, *86*, 123509.
59. Bisquert, J.; Fabregat-Santiago, F., Impedance Spectroscopy: *A General Introduction and Application to Dye-Sensitized Solar Cells*; CRC Press: Boca Raton, FL, 2010.
60. Leever, B. J.; Bailey, C. A.; Marks, T. J.; Hersam, M. C.; Durstock, M. F. *In Situ* Characterization of Lifetime and Morphology in Operating Bulk Heterojunction Organic Photovoltaic Devices by Impedance Spectroscopy. *Adv. Energy Mater.* **2012**, *2*, 120–128.
61. Tang, H.; Prasad, K.; Sanjinès, R.; Schmid, P. E.; Lévy, F. Electrical and Optical Properties of TiO_2 Anatase Thin Films. *J. Appl. Phys.* **1994**, *75*, 2042–2047.
62. Koster, L. J. A.; Shaheen, S. E.; Hummelen, J. C. Pathways to a New Efficiency Regime for Organic Solar Cells. *Adv. Energy Mater.* **2012**, *2*, 1246–1253.
63. Street, R. A.; Schoendorf, M.; Roy, A.; Lee, J. H. Interface State Recombination in Organic Solar Cells. *Phys. Rev. B* **2010**, *81*, 205307.
64. Garcia-Belmonte, G.; Bisquert, J. Open-Circuit Voltage Limit Caused by Recombination through Tail States in Bulk Heterojunction Polymer-Fullerene Solar Cells. *Appl. Phys. Lett.* **2010**, *96*, 113301.
65. Burke, T. M.; McGehee, M. D. How High Local Charge Carrier Mobility and an Energy Cascade in a Three-Phase Bulk Heterojunction Enable >90% Quantum Efficiency. *Adv. Mater.* **2014**, *26*, 1923–1928.
66. Jamieson, F. C.; Domingo, E. B.; McCarthy-Ward, T.; Heeney, M.; Stingelin, N.; Durrant, J. R. Fullerene Crystallisation as a Key Driver of Charge Separation in Polymer/Fullerene Bulk Heterojunction Solar Cells. *Chem. Sci.* **2012**, *3*, 485–492.